Rain Drop Size Distributions Estimated from NOAA Snow-Level Radar Data

PAUL E. JOHNSTON,[a,b] CHRISTOPHER R. WILLIAMS,[c] AND ALLEN B. WHITE[b]

[a] *Cooperative Institute for Research in Environmental Sciences, University of Colorado Boulder, Boulder, Colorado*
[b] *NOAA/Physical Sciences Laboratory, Boulder, Colorado*
[c] *Colorado Center for Astrodynamics Research, Ann and H. J. Smead Aerospace Engineering Sciences, University of Colorado Boulder, Boulder, Colorado*

(Manuscript received 21 April 2021, in final form 17 December 2021)

ABSTRACT: Using NOAA's S-band High-Power Snow-Level Radar (HPSLR), a technique for estimating the rain drop size distribution (DSD) above the radar is presented. This technique assumes the DSD can be described by a four parameter, generalized gamma distribution (GGD). Using the radar's measured average Doppler velocity spectrum and a value (assumed, measured, or estimated) of the vertical air motion w, an estimate of the GGD is obtained. Four different methods can be used to obtain w. One method that estimates a mean mass-weighted raindrop diameter D_m from the measured reflectivity Z produces realistic DSDs compared to prior literature examples. These estimated DSDs provide evidence that the radar can retrieve the smaller drop sizes constituting the "drizzle" mode part of the DSD. This estimation technique was applied to 19 h of observations from Hankins, North Carolina. Results support the concept that DSDs can be modeled using GGDs with a limited range of parameters. Further work is needed to validate the described technique for estimating DSDs in more varied precipitation types and to verify the vertical air motion estimates.

KEYWORDS: Drop size distribution; Algorithms; Profilers, atmospheric; Precipitation; Radars/Radar observations

1. Introduction

Radar measurements of precipitation have a long history. Radars have the ability to monitor large volumes while providing high temporal and spatial resolutions. This allows more representative precipitation observations than the point or small-volume measurements made by rain gauges and disdrometers. Understanding the relationship between radar measurables and geophysical quantities is a broad area of research. Work remains unfinished in retrieving the rain drop size distribution (DSD) from radar measurements.

Marshall, Hitchfield, and Gunn presented a broad overview of the subject in 1955 (Marshall et al. 1955). In their overview, the relationship between radar reflectivity factor Z ($\text{mm}^6\ \text{m}^{-3}$) and rainfall rate R ($\text{mm}\ \text{h}^{-1}$), known as the Marshall–Palmer (MP) relationship, $Z = 200R^{1.6}$, was presented, which is slightly different than the relationship presented earlier in Marshall and Palmer (1948). These papers used an exponential DSD to describe raindrop size measurements obtained using dye-covered paper located under the fixed volume of an S-band radar (Marshall et al. 1947). This relationship described the large-drop end of the DSD that produces most of the reflectivity observed by the radar.

Atlas et al. (1973) presented an overview of the basic theory and formulation of relationships between radar observations and rain drop size distributions. Atlas et al. (1973) again described the DSD using the exponential distribution.

The relationship $v_{\text{fall}}(D)$ between drop size D (mm) and the drop terminal fall speed v_{fall} ($\text{m}\ \text{s}^{-1}$) is a crucial part of drop size science. Throughout this document, D is the equivalent liquid spherical drop diameter for a given mass of water, in millimeters. Falling raindrops have an oblate shape when falling, yet, when viewed from the bottom, they appear circular on average. Gunn and Kinzer (1949) is the standard source of this relationship. These U.S. Weather Bureau scientists made very detailed and precise measurements of the fall velocity of water drops indoors under carefully controlled conditions.

The DSD is expressed as $N(D)$ ($\text{m}^{-3}\ \text{mm}^{-1}$), representing the number of drops per cubic meter per unit size. Early studies modeled the DSD as an exponential distribution. The exponential DSD, $N_e(D) = N_0 e^{-\Lambda D}$, is a two-parameter distribution with parameters N_0 ($\text{m}^{-3}\ \text{mm}^{-1}$) and the scale parameter Λ (mm^{-1}). In the 1980s, the gamma distribution (Ulbrich 1983) became a common descriptor of DSDs, since they more accurately describe observations. The gamma DSD, $N_G(D) = N_0 D^{\mu} e^{-\Lambda D}$, is a three-parameter distribution with parameters N_0 ($\text{m}^{-3}\ \text{mm}^{-1-\mu}$), the shape parameter μ (unitless), and Λ (mm^{-1}). Recently, improved observations show that the gamma distribution is not adequate to describe the entire DSD (Thurai et al. 2017), especially the small drop, or drizzle part of the DSD. More recently, the generalized gamma distribution (GGD) has become a common representation for DSDs (Thurai et al. 2019; Raupach et al. 2019; Currier et al. 1992). The GGD is a four-parameter distribution, $N_{\text{GGD}}(D) = N_0(\Lambda D)^{c\mu-1} e^{-(\Lambda D)^c}$, with parameters N_0 ($\text{m}^{-3}\ \text{mm}^{-1-\mu}$), μ (unitless), c (unitless), and Λ (mm^{-1-c}). These three distributions are related. If c is set to 1 in $N_{\text{GGD}}(D)$ it becomes a gamma distribution. In a similar fashion, $N_e(D)$ results from setting $\mu = 0$ in the gamma DSD, $N_G(D)$.

Other distributions have been used to describe DSDs, such as the lognormal distribution and Weibull distributions. The two-parameter exponential distribution, three-parameter gamma distribution, the Weibull distribution, lognormal distribution, Rayleigh distribution, and chi distribution are

Corresponding author: Paul E. Johnston, Paul.E.Johnston@noaa.gov

DOI: 10.1175/JTECH-D-21-0049.1

special cases of the generalized gamma distribution (Stacy 1962). We use the GGD since it is becoming widely used and describes the observations.

Thurai et al. (2017), Raupach et al. (2019), and Thurai et al. (2019) show that the small drop size portions ($D < 0.5$ mm) of many DSD measurements are missing. This "drizzle" part of the DSD is not well described using the gamma DSD model. Raupach et al. (2019) and Thurai et al. (2019) show that the full DSD can be represented using the GGD model. They also suggest that DSDs can be described using a GGD with constant, or universal, values for the parameters μ and c. This work uses $N_{GGD}(D)$ to describe the DSD.

Data from the NOAA High-Power Snow-Level Radar (HPSLR) are used to estimate DSDs described with the $N_{GGD}(D)$ model. In these retrievals, vertical air velocity w is specified for each retrieval. Three different methods to specify w are presented. In many cases, the drizzle mode (diameter range of 0.001–0.5 mm) is observed. Statistics of the retrieved μ and c parameters support the concept of universal DSD.

2. Method

The HPSLR, developed at NOAA Physical Sciences Laboratory, is identical to the instrument described in Johnston et al. (2017) except the output power is 10 W instead of 1 W. The HPSLR is a frequency-modulated continuous wave (FM-CW) radar operating at 2835 MHz, with fixed vertically pointing antennas. The transmit and receive antennas are identical 1.2-m parabolic reflectors with 6° beamwidths. This S-band frequency has a wavelength of 10.6 cm.

The data for this work were obtained when the HPSLR was near Hankins, North Carolina (35.731°N, 82.0271°W), on 19 April 2014. All times and dates are UTC. The HPSLR operated with 40 m vertical resolution. Data were sampled for 28.67 s each dwell. Due to data processing overhead, each dwell took 37.6 s. For this analysis, four radar dwells were averaged into 150-s averages, representing 114.7 s of data. Each average power spectra contain 256 points, with a full-scale Doppler velocity of 23.60 m s^{-1}. The first sampled range for this radar is centered 40 m above the radar. Data from 350 heights were processed, giving samples every 40 m to 14 km above the radar. This work utilizes the lower 2000 m of HPSLR range altitudes (50 heights), limiting the data to liquid precipitation, thus avoiding data near the bright band where there are mixed-phase particles. This dataset consists of 574 observations covering the entire day. The data used for this analysis were limited to data with a radar reflectivity factor of $10\log_{10}(Z) \geq 0.0$ dBZ.

This work builds on the work of Williams (2002). One major change is the use of the four-parameter GGD instead of the three-parameter gamma distribution. The second major change is the use of a different technique to determine the vertical air motion. The vertical air motion, w, follows standard meteorological convention, with upward motion being positive. The Doppler velocity and the raindrop fall velocity $v_{fall}(D)$ are positive downward. For this document for all velocities are in units of meters per second.

The starting point for estimating the $N(D)$ from a vertically pointing radar is the reflectivity spectral density z' [Atlas et al. 1973, Eq. (16)]:

$$z'\left[r, v_{fall}(r, D)\right] = N(D)D^6 dD/dv_{fall}. \quad (1)$$

The distance from the radar to the scattering volume is the range r (m). For each range the HPSLR processes the received backscatter from the raindrops to get an average power spectrum $S(v_{fall})$. This power spectrum contains observations of z' [r, $v_{fall}(r, D)$] for a volume centered at r. This volume is determined by the parameters of the radar. These observations are related to $N(D)$ through the drop fall speed $v_{fall}(r, D)$ and range shown in Eq. (1).

The HPSLR averaged power spectrum is scaled such that the sum of the values gives the radar reflectivity factor Z (mm^6 m^{-3}):

$$Z = \sum S(v_{fall}). \quad (2)$$

The reflectivity spectral density is then estimated from the spectrum:

$$z'(v_{fall}) = \frac{S(v_{fall})}{\Delta v}. \quad (3)$$

The width of the spectral bins Δv is determined by the wavelength of the radar λ (m), the number of points in the spectrum n_{DFT}, and the intersweep period τ_{IPP} (s) used to acquire the data (IPP is used to denote the intersweep period to keep the terminology analogous to the pulsed radar systems the authors also utilize). For this dataset $\Delta v = 0.1844$ m s^{-1}:

$$\Delta v = \frac{\lambda}{2\tau_{IPP} n_{DFT}}. \quad (4)$$

Equation (1) can be combined with Eqs. (2) and (3) to show relationships between the observed spectrum and the target DSD:

$$Z = \sum_{v_{min}}^{v_{max}} S(v_{fall}) = \sum_{v_{min}}^{v_{max}} z'(v_{fall})\Delta v_{fall}$$

$$= \sum_{d_{min}}^{d_{max}} N\left[D(v_{fall})\right] D(v_{fall})^6 \Delta D(v_{fall}). \quad (5)$$

Since the HPSLR measures Doppler velocity $v_{Doppler}$, which is the raindrop fall speed plus atmospheric motion equation [Eq. (1)] is modified to account for vertical air motion $w(r)$. The HPSLR is pointed vertically so range r and height above ground are equivalent:

$$z'(r, v_{fall}) = N\{D\left[v_{DOPPLER} + w(r)\right]\} D\left[v_{DOPPLER} + w(r)\right]^6 \times \frac{dD\left[v_{DOPPLER} + w(r)\right]}{dv}. \quad (6)$$

The drop size D is a function of the fall velocity, $v_{fall} = v_{DOPPLER} + w(r)$, which changes with height due to

decreasing air density. As described above, w is defined in the opposite sense of v_{fall}.

In Eq. (6), the drop size D is a function of the terminal velocity v_{fall} and the height above mean sea level (MSL), which is obtained from the range value r and the altitude of the radar site. The foundation of the technique is the existence of a relationship between drop fall velocity and drop size. Gunn and Kinzer (1949) was done near sea level, in Washington, D.C. (1013 hPa, 20°C). Gunn and Kinzer (1949) measured drops with diameters for 0.1–5.8 mm. Equation (6) shows that the relationship between the radar spectral data depends on the fall velocity relationship, and the derivative of this function. For the rest of this document the dependance on range and height will be implicit to simplify the notation.

Several relationships have been developed to express drop fall velocity measurements as empirical functions. One commonly used relationship, and its derivative, comes from Atlas et al. (1973):

$$v_{\text{Atlas}}(D) = 9.65 - 10.3e^{-0.6D} \quad \frac{dv_{\text{Atlas}}(D)}{dD} = 6.18e^{-0.6D}. \tag{7}$$

Foote and Du Toit (1969), did a careful fitting to the Gunn and Kinzer (1949) data, and found a ninth-order polynomial gives an accurate relationship:

$$v_{\text{Foote}}(D) = \sum_{i=0}^{9} b_i D^i \quad \frac{dv_{\text{Foote}}(D)}{dD} = \sum_{i=1}^{9} i b_i D^{i-1}. \tag{8}$$

Brandes et al. (2002) fitted data using a fourth-order polynomial. This function is valid for drop diameters smaller than 8 mm:

$$v_{\text{Brandes}}(D) = \sum_{j=0}^{4} b_j D^j \quad \frac{dv_{\text{Brandes}}(D)}{dD} = \sum_{j=1}^{4} i b_j D^{j-1}. \tag{9}$$

There are some problems with these relationships. The original Gunn and Kinzer (1949) data have a maximum drop size of 5.8-mm diameter. Larger drops are known to exist. Thurai and Bringi (2005) used an 80-m-high bridge in Austria to measure the drop size–velocity relationship. Their data show that for drops larger than 7 mm, the velocity can decrease with increasing drop diameter, which is captured in (9). This makes the Brandes et al. (2002) relationship attractive. However, since this technique requires sorting of the drops by velocity, using the multivalued part of the relationship presents a problem. Our solution is to limit the maximum drop size. A second problem is that the derivative dv_{fall}/dD gets very small (or even zero) for large drops. This presents a problem in Eq. (1), where the solution can become unstable for very large drops.

Figure 1 shows the large drop size end of the Brandes et al. (2002) relationship in Eq. (9). We choose to limit the maximum drop size to the largest value of the monotonic function, limiting the largest drop to 5.35 mm. This appears to be a limitation, but in practical terms it does not limit the method. A large study of disdrometer data (Gatlin et al. 2015) showed

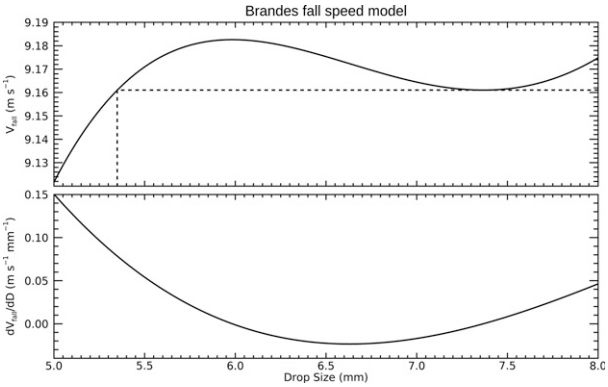

FIG. 1. Details of the Brandes et al. (2002) fall velocity relationship for large drops. (top) The fall velocity as a function of the drop size. The dashed line shows the maximum unambiguous drop size of 5.34 979 mm, with the corresponding maximum unambiguous fall velocity of 9.161 035 m s^{-1}. (bottom) The derivative of the fall speed with respect to the drop size.

that 0.4% or fewer observed raindrops were larger than 5 mm. Figure A.1c of Gatlin et al. (2015) shows a similar result, with the velocity of large drops not following an increasing function.

These relationships show drop fall velocities at sea level. Above the surface the fall velocity increases due to the decrease in atmospheric density. Foote and Du Toit (1969) and others note that at lower densities drops fall faster, requiring modification of the $v_{\text{fall}}(D)$ formulation. The drop fall speed $v(h)$ at height h (m) above a reference level can be related to drop fall velocity at the reference level v_0, the density at the reference level ρ_0, and the density at the height of the drop $\rho(h)$ is expressed by the relationship

$$v(h) = \left[\frac{\rho_0}{\rho(h)}\right]^m v_0. \tag{10}$$

Foote and Du Toit (1969) use a value of $m = 0.4$. Beard (1985) presents a simple analysis showing that the exponent should be a function of the drop size:

$$m(D) = 0.375 + 0.025D. \tag{11}$$

We use the latter relationship in our fall speed corrections.

Density ρ is a function of pressure, humidity, and temperature, which are not always available at the radar site. For the density ratio of (10), we use an exponential model to relate density at the geometric height h to density at the surface:

$$\rho(h) \approx \rho_0 e^{-h/H_\rho}. \tag{12}$$

Here, the reference level is MSL, so h becomes height above MSL. Looking at Eq. (45) in the *U.S. Standard Atmosphere, 1976* (COESA 1976), in the lower troposphere (<10 km), the density scale height H_ρ is equal to the pressure scale height. The pressure scale height is a function of gravity, longitude, humidity, and temperature (see, for example, Bradley and Fairall 2006, section A6). For midlatitudes and temperatures

around 10°C, a value of 8300 m is a reasonable value for the density scale height. A constant density scale height is utilized in this demonstration of the retrieval technique. In a more precise application, variations of temperature, pressure, and humidity with height could be used to determine the density.

The height corrected fall speed can be written as a function of the drop size D and the height above sea level h (m):

$$v_{\text{fall}}(D,h) = v_{\text{fall}}(D,h_0)\left[\frac{\rho_0}{\rho(h)}\right]^{m(D)} \approx v_{\text{fall}}(D,h_0)\left(\frac{\rho_0}{\rho_0 e^{-h/H_\rho}}\right)^{m(D)}$$

$$= e^{h(0.375+0.025D)/H_\rho} v_{\text{fall}}(D,h_0)$$

$$\frac{dv_{\text{fall}}(D,h)}{dD} = e^{h(0.375+0.025D)/H_\rho}\left[v_{\text{fall}}(D,h_0)\frac{h(0.025)}{H_\rho} + \frac{dv_{\text{fall}}(D,h_0)}{dD}\right]. \quad (13)$$

One difficulty using Eq. (9) is that it is not easily invertible to get a drop size as a function of velocity relation. Instead of solving for $D(v_{\text{fall}})$ algebraically, a Newton–Raphson method (Press et al. 1992) is used to get $D(v_{\text{fall}})$ to within some small increment. The convergence tolerance ε is set very small ($\varepsilon = 5 \times 10^{-15}$ mm) to minimize drop size errors. This method ensures that the drop size to velocity relationships are well defined in both the forward and reverse directions. The Newton–Raphson method requires very few iterations to converge on a solution, typically fewer than eight iterations.

After accounting for the vertical air motion, the Doppler spectral density observations are converted to $N(D)D^6$ by modifying Eq. (1) and applying to each spectral point i:

$$N(D_i)D_i^6 = z_i'(v_{\text{fall}_i})dV/dD = \frac{S_i(v_{v_{\text{fall}_i}})}{\Delta v}\frac{dv_{\text{fall}}}{dD}\bigg|_{D_i}. \quad (14)$$

We model the observed DSD using a GGD. Since the observation is in D^6 space, we express the model in the same space:

$$D^6 N_{\text{GGD}}(D) = D^6 N_0 (\Lambda D)^{c\mu-1}\exp\left[-(\Lambda D)^c\right]$$

$$= N_0(\Lambda^{-6})(\Lambda D)^{c\mu+5}\exp\left[-(\Lambda D)^c\right]. \quad (15)$$

A nonlinear least squares fit in logarithmic space, minimizing the squared difference between the input data and the $N_{\text{GGD}}(D)$ model, χ^2, is used to determine the $N_{\text{GGD}}(D)$ that best describes the radar data. The vertical air velocity w is specified as an input value to convert the input data from Doppler velocity to drop fall speed:

$$\chi^2 = \sum_{i=1}^{n}\left\{\ln\left[\frac{S_i(v_{\text{fall}_i})}{\Delta v}\frac{dV}{dD}\bigg|_{D_i}\right] - \ln\left\{N_0\Lambda^{-6}(\Lambda D_i)^{c\mu+5}\exp\left[-(\Lambda D_i)^c\right]\right\}\right\}^2. \quad (16)$$

This is minimized by solving the four equations, where $x = N_0, \mu, \Lambda, c$:

$$0 = \sum_1^n\left\{\left(\ln\left[\frac{S_i(v_{\text{fall}_i})}{\Delta v}\frac{dV}{dD}\bigg|_{D_i}\right] - \ln\left\{N_0\Lambda^{-6}(\lambda D_i)^{c\mu+5}\exp\left[-(\Lambda D_i)^c\right]\right\}\right)\times\left\{\frac{\delta\ln\left\{N_0\Lambda^{-6}(\lambda D_i)^{c\mu+5}\exp\left[-(\Lambda D_i)^c\right]\right\}}{\delta x}\right\}\right\}. \quad (17)$$

The derivative with respect to N_0 is relatively easy to perform, giving a solution for N_0 given the input data and the other variables:

$$n\ln N_0 = \sum_1^n\ln\left[\frac{S_i(v_{\text{fall}_i})}{\Delta v}\frac{dv_{\text{fall}}}{dD}\bigg|_{D_i}\right] - \sum_1^n\ln\left\{(\Lambda^{-6})(\Lambda D_i)^{c\mu+5}\exp\left[-(\Lambda D_i)^c\right]\right\}. \quad (18)$$

Using this to determine N_0 reduces the nonlinear problem to three parameters μ, Λ, and c. We use the Levenberg–Marquardt method to solve for these parameters (Markwardt 2009). This implementation does discrete differentiation, so the derivatives do not need to be explicitly put into the routine. This routine provides a good estimate of the parameters, given the HPSLR data, vertical air velocity w, and a reasonable estimate of the starting value of the parameters: $\mu = -0.46$, $\Lambda = 1.0$, and $c = 3.0$.

The inputs to the DSD estimation routine consist of average power spectra from the radar, and values of the vertical air velocity w. These spectra have been calibrated using the technique detailed by Hartten et al. (2019). This technique adjusts radar calibration such that radar accumulated precipitation using a Z–R relationship matches the accumulation from a tipping-bucket rain gauge. Additional corrections for volume mismatch and gain variations in range, as detailed in Johnston et al. (2017), are also included in the calibration.

3. Example of radar derived DSD

The technique is best described with an example. Using the Hankins HPSLR data from 19 April 2014 each Doppler spectrum was evaluated to get an $N_{\text{GGD}}(D)$ model using the method described by (15)–(18). The data cover 574 time periods and 50 heights. Figure 2 shows the spectrum and model with the smallest χ^2 value obtained. Describing the information in the plot explains the technique and the information derived from the technique.

In all three panels, the dots represent the observed radar data points used to create the model DSD. The bottom panel shows the input spectrum and the model DSD spectrum obtained from fitting the GGD to the data. The dark solid line shows the input power spectrum, using the linear power scale on the left of the panel. The lighter solid line shows the input power spectrum using logarithmic scaling (dB) shown with the scale on the right side. The dotted lines show the model DSD converted to the Doppler velocity domain. The

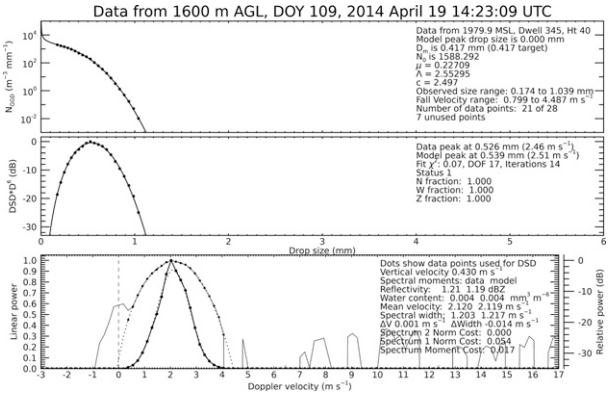

FIG. 2. An example of the fitting of the radar spectrum to a DSD. This spectrum was chosen since it shows the best χ^2 value of the entire dataset. (middle),(bottom) Normalized data. (top) The DSD values.

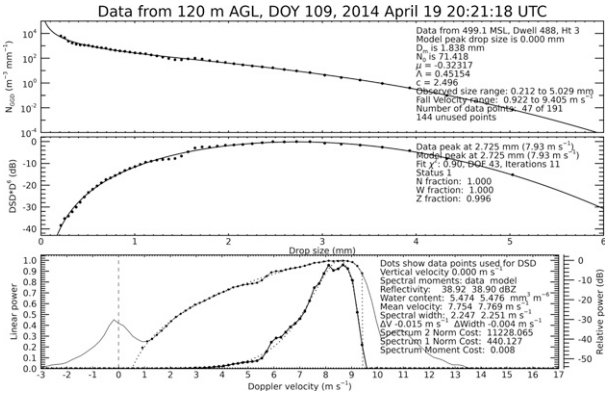

FIG. 3. An example spectrum with large reflectivity. For this solution the w was assumed to be zero. (middle),(bottom) Normalized data. (top) The DSD values.

spectra have been normalized to the largest peak of either the model or observed data, so relative amplitudes are maintained. In the logarithmic spectrum, regions where there is no signal are seen as dropouts.

The middle panel shows the spectral values converted into $N(D)D^6$ space as points. The solid line shows the model DSD that is the least squares fit to the data. As in the bottom panel, these curves are normalized to the largest of the maximum value of the data and model, so relative sizes are preserved. The top panel shows the DSD in absolute numbers. As in the middle panel, the points show the data, and the solid line shows the model.

The text at the right of each panel shows the fitted parameters and fitting statistics. In this example the fitted parameters are $\mu = 0.23$, $\Lambda = 2.55$, and $c = 2.50$. There are 28 points in the signal spectrum, 21 of which are used for the data fitting. The values in the lower panel show the vertical air velocity was set to 0.43 m s^{-1}. This is the vertical air velocity determined using the $D_m(Z)$ relationship explained later in this manuscript.

The signal spectrum is the received power spectrum with the mean noise level removed. In a perfect system, the signal would be defined as all the points around the peak that are above zero. In practice, there are other signals in the spectrum that need to be removed from the signal spectrum used for the creation of the DSD. In many cases, as seen in Figs. 2 and 3, there are a strong signals at zero velocity caused by ground clutter. In addition, there are unidentified signals at other frequencies that need to be removed, also seen in Figs. 2 and 3. To isolate the precipitation signal the assumption is made that the precipitation is the largest signal in the spectrum. The maximum of the spectrum, then the lower, and the upper edges of the signal are located. Searching from the maximum signal, the signal values are required to decrease as the signal is farther from the signal maximum. When a minimum is detected more than 11 dB below the peak that point is identified as the end of the precipitation signal. This allows local minima near the peak to remain in the signal. In cases where the local minimum occurs within four spectral points of the zero Doppler velocity, as seen in Fig. 2, the point at the minimum is reduced by a factor of 2. This assumes the minimum is the sum of two equal signals, one ground clutter and one the precipitation signal. Signals that are not precipitation sometimes occur near the high velocity edge of the precipitation region of the spectrum. To exclude these interfering signals, the curvature of the spectrum is required to be negative for large velocity signals smaller than 30 dB below the peak. To be accepted for DSD model retrieval, at least 20 drop sizes in the precipitation region are required in the DSD obtained from the spectrum.

Various measured values and cost function estimates are shown in the text of the panels. These values are defined in Table 1. These definitions can be found in Tapiador et al. (2014) and Williams and Gage (2009). The example shown in Fig. 2 demonstrates the sensitivity of the HPSLR, showing a very good fit of the model to data with small reflectivity.

4. Need for verification data

The results in Fig. 2 appear reasonable but need verification. The radar measures the Doppler velocities of the raindrops. The determination of the rain drop distribution within the radar sample volume using (14) requires the drop fall speeds, which are the sum of the Doppler velocities and w. This section explores the determination of the vertical air velocity w.

The retrieval technique described above is similar to the DSD retrieval technique using the Micro Rain Radar (MRR) (Peters et al. 2005). One difference is that the MRR technique assumes $w = 0$ and the analysis presented in Peters et al. (2005) quantifies the DSD errors using this assumption. Adiros et al. (2016) present results comparing MRR DSDs with 2DVD disdrometer DSDs and conclude that the $w = 0$ assumption does cause uncertainties to the DSD retrievals, but the retrieved DSDs obtained still provide useful insight into microphysical processes aloft.

As an example of retrieving the DSD with the $w = 0$ assumption, Fig. 3 shows the model fitting the data from the

TABLE 1. Formulas and symbol definitions for quantities shown in the plots of the DSDs and data. Unreferenced equations were formulated by the authors.

Symbol	Definition	Units		Source
D_m	Mean mass-weighted drop diameter	mm	$D_m \equiv M_{4,3} = \dfrac{\int N(D)D^4 dD}{\int N(D)D^3 dD}$	Tapiador et al. (2014) (26)
N fraction	Fraction of DSD covered by data		$\dfrac{N_{\text{observed}}}{N_{\text{Total}}} = \dfrac{\sum_{D=D_{\min}}^{D_{\max}} N_{\text{Model}}(D_i)\Delta D}{\sum_{D=0.001}^{D=8\text{mm}} N_{\text{Model}}(D_i)\Delta D} = \dfrac{\sum_{D=D_{\min}}^{D_{\max}} N_{\text{Model}}(D_i)}{\sum_{D=1}^{D=8000\text{m}} N_{\text{Model}}(D_i)}$	—
W	Water content	mm^3 m^{-6}	$W \equiv \dfrac{\pi}{6000}\int n(D)D^3\, dD \approx \dfrac{\pi}{6000}\sum_{i=1}^{8000} N(i\Delta D)(i\Delta D)^3 \Delta D$	Tapiador et al. (2014) (20)
W fraction	Fraction of W covered by data	—	$\dfrac{W_{\text{Observed}}}{W_{\text{Model}}} = \dfrac{\sum_{i=\min}^{\max} N(D_i)(D_i)^3}{\sum_{i=1}^{8000} N(D_i)(D_i)^3}$	—
$\langle V \rangle$	Mean Doppler velocity	m s^{-1}	$\langle V \rangle = \dfrac{\sum_{i=V_{\min}}^{i=V_{\max}} V_i S_i}{\sum_{i=V_{\min}}^{i=V_{\max}} S_i}$	Carter et al. (1995)
ΔV	Velocity difference	m s^{-1}	$\Delta V = \langle V_{\text{Observed}} \rangle - \langle V_{\text{Model}} \rangle$	—
W	Spectral width	m s^{-1}	$W = 2\sqrt{\dfrac{\sum_{i=V_{\min}}^{i=V_{\max}} (V_i - \langle V \rangle)^2 S_i}{\sum_{i=V_{\min}}^{i=V_{\max}} S_i}}$	Carter et al. (1995)
ΔW	Spectral width difference	m s^{-1}	$\Delta W = W_{\text{Observed}} - W_{\text{Model}}$	—
$J_{\|\text{spectra}\|}$	Spectrum 2 norm cost	—	$J_{\|\text{spectra}\|} = \sum_i \left[S_{\text{Observed}}(v_i) - S_{\text{Model}}(v_i)\right]^2$	Williams and Gage (2009) (16)
$J_{\|\text{spectra}\|}$	Spectrum 1 norm cost	—	$J_{\|\text{spectra}\|} = \sum_i \left\|S_{\text{Observed}}(v_i) - S_{\text{Model}}(v_i)\right\|$	Williams and Gage (2009) (17)
J_{moment}	Spectrum moment cost	—	$J_{\text{moment}} = \dfrac{\|Z_{\text{observed}} - Z_{\text{Model}}\|}{Z_{\text{observed}}} + \dfrac{\|\langle V_{\text{observed}} \rangle - \langle V_{\text{Model}} \rangle\|}{\langle V_{\text{observed}} \rangle} + \dfrac{\|W_{\text{observed}} - W_{\text{Model}}\|}{W_{\text{observed}}}$	Williams and Gage (2009) (18)

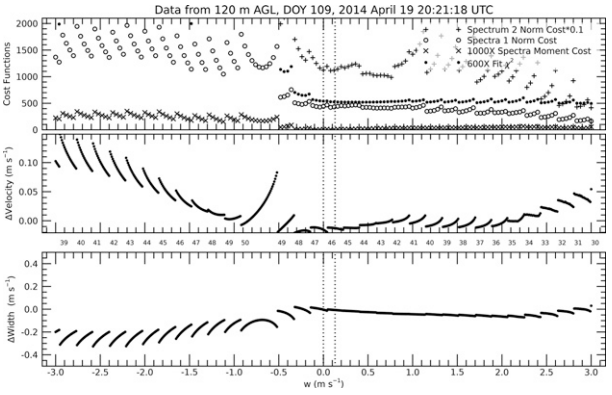

FIG. 4. Plots of different measures of goodness of fit that might be used to select the model that best describes the DSD for the input data. (top) To make the data more visible, only every third value has been shown. The numbers between the middle and bottom panels show the number of data points used to fit the model. The dashed vertical lines indicate two solutions discussed in the text.

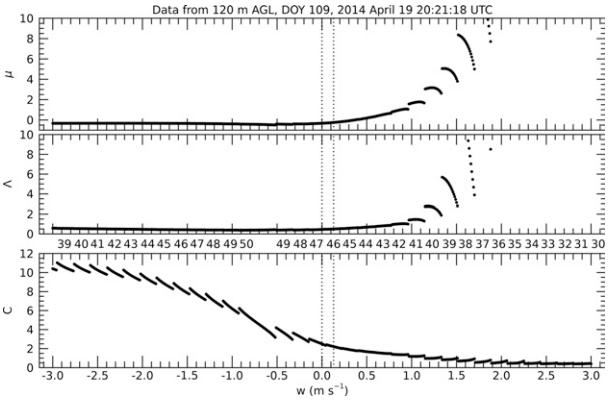

FIG. 5. Model parameters as a function of the vertical velocity used to determine the fall speed of the drops. The dashed vertical lines indicate two solutions discussed in the text.

120-m height at 2021:18 UTC 19 April 2014. This example has larger reflectivity (39 dBZ) than the example presented in Fig. 2. The retrieved DSD appears reasonable both in a "fit-by-eye" sense, and in the values of the cost functions, which are defined in Table 1. The difference in the mean radial velocity between the model and the data is 0.015 m s^{-1}, which is much less than the spectral bin width of 0.1844 m s^{-1}.

The question remains though, is this DSD a good representation of the raindrops in the radar volume? To explore the effects of different values of w, DSDs were retrieved from the Doppler spectrum and modeled to get $N_{GGD}(D)$ with w varying from -3.0 to 3.01 m s^{-1}. Using an increment of 0.01 m s^{-1} in w gives 602 different retrieved DSDs and models. Figure 4 shows the results for the spectrum shown in the bottom panel of Fig. 3.

Figure 4 shows cost functions for each of the 602 different retrieved DSDs and $N_{GGD}(D)$ models. The top panel shows the χ^2 value and statistics from the analysis routines. These cost functions are described by Williams and Gage (2009) and defined in Table 1. Each segment comes from using a different number of data values in the fitting. The number of data values used for the model fit is shown between the bottom two panels. For $-0.5 < w < 1.0$ m s^{-1}, the cost functions shown in the top panel are relatively constant. The second panel shows the difference of the velocity moments measured with the observed data and the modeled spectrum. The third panel shows the difference in the spectral widths. For both the velocity and spectral width moments, the calculations are done using the data values used for the fitting of the model, so are not the velocity moment observed from the entire set of signal points. Three important conclusions arise from this analysis:

1) The χ^2 cost function is nearly constant for a wide range of vertical air motions making χ^2 a poor choice for selecting a value of w that describes the atmospheric state. Small values of χ^2 indicate that the $N_{GGD}(D)$ model represents the data well. The other cost functions exhibit similar behavior: small cost function values show the model represents the data well, but there is no obvious cost value that can be used to determine w.
2) Both the first and second moments of the observed spectrum and the modeled spectrum are well represented over a wide range of w, making these poor criteria for selecting the best fit to the data.
3) The previous two conclusions about Fig. 4 suggest that the GGD model is unconstrained and can adapt to a wide variety of DSD shapes.

Figure 5 shows the GGD parameters determined by the fitting of the data to the model. The displayed values of μ, Λ, and c do not show the entire set of retrieved values. As observed in Fig. 4 with small-valued cost functions, there are large ranges in w where the μ and Λ parameters are nearly constant. Selecting a fit based on values of the $N_{GGD}(D)$ parameters could be insensitive to the vertical air motion, making selection of the proper value of w difficult.

Figure 6 shows how the retrieved drop sizes change with different vertical air velocity inputs. The sizes of the smallest (D_{min}) and largest (D_{max}) drops retrieved and the mean mass-weighted drop size D_m all show a monotonic relationship with the vertical velocity. The values of D_{min} and D_m display some minor discontinuities for values of $w < -0.5$ m s^{-1}. These discontinuities are related to the discrete values of the velocities of the input spectrum (shown in Fig. 3). Since the maximum drop size is fixed by the fall velocity to drop size relationship, the maximum size oscillates as the data value of the largest drop is moved in the solution. The value of D_m is computed from the model $N_{GGD}(D)$ using the formula shown in Table 1 and is monotonic with w.

As the vertical air velocity increases, both D_{min} and D_m increase. The reflectivity factor Z (mm^6 m^{-3}) and the mass-weighted mean drop diameter D_m (mm) are correlated. Williams et al. (2014) show in their Fig. 4a relationship between Z and D_m:

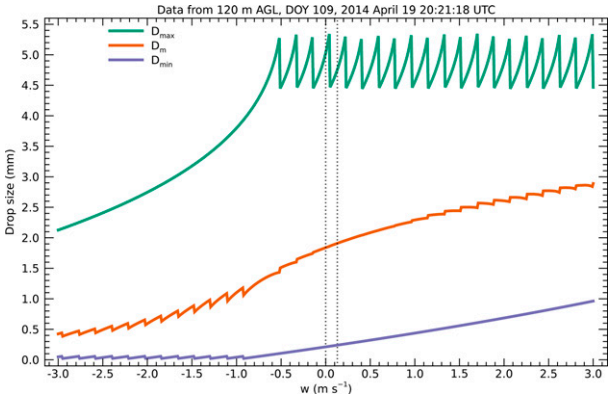

FIG. 6. Different measures of drop sizes with different values of vertical motion. The lower curve shows the smallest drop size measured. The upper curve shows the largest size drop measured. The middle curve shows the mean mass weighted drop diameter D_m determined from the GGD model for this input spectrum. The dashed vertical lines indicate two solutions discussed in the text.

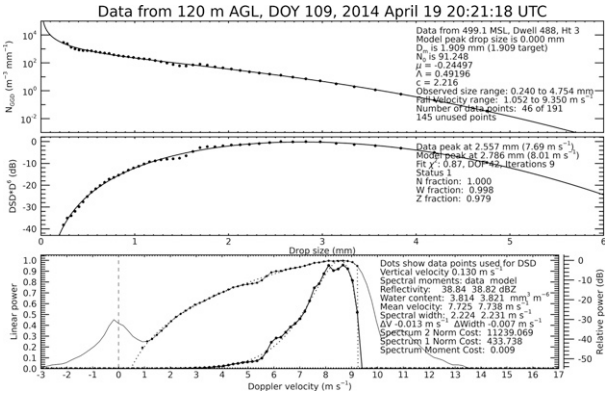

FIG. 7. In this solution the vertical velocity was set to the value giving a $D_m = 1.909$ mm. (middle),(bottom) Normalized data. (top) The DSD values. These are the same data as shown in Fig. 3, with w determined using the $D_m(Z)$ relationship.

$$D_m(Z) = \left(\frac{Z}{194}\right)^{1/5.71} \text{ mm}. \tag{19}$$

Using this value of D_m allows determination of the DSD without knowing w, which than can be modeled to get a $N_{GGD}(D)$ that represents the data.

Using the same data as Fig. 3, Fig. 7 shows the DSD determined by searching for the vertical air velocity that gives the mean mass-weighted drop size D_m that corresponds to the observed reflectivity Z using Eq. (19). As seen in Figs. 2, 3, and 7, not all spectral values are used to determine the DSD, which is then modeled. The target value of D_m is determined using the reflectivity Z of the data points used to determine the model. This allows direct comparison of Z and D_m between the data and the model. This also removes some of the contamination from ground clutter and other nonprecipitation signals that can affect the Z value, especially in small Z cases. To determine the target D_m value, a search of the $N(D)D^6$ sets resulting from input values of $w = 4.0$ m s^{-1} is conducted. The search is conducted using steps of $\Delta v/3$ [see (4)]. The $N(D)D^6$ set with the largest value of Z is used to set the target D_m value. The initial value of w is determined from the Doppler velocity of the maximum spectral value of the set:

$$w_{\text{initial}} = v_{\text{Doppler}}\{\max[S(v)]\} - v_{\text{fall}}[1.5D_m(Z)]. \tag{20}$$

This approach is easier to implement than a search for a minimum cost function, or some other criteria, since the target D_m for a given spectrum can be found without fitting the model to the data, but instead by finding the set of drop sizes with the largest Z. The retrieval with that target D_m value is found by fitting the model with different values of the w, starting with w_{initial}. Since $D_m(w)$ is monotonic the search is done with a simple bracket and bisect technique, an easy search to perform. The search is limited to finding D_m within 0.0005 mm of the target value, or to 50 iterations, whichever occurs first. When the search is limited by the number of iterations, a solution is accepted if the final D_m value is within 0.05 mm of the target value of D_m determined by Eq. (19). Figure 6 shows there are minor discontinuities when the number of points used in the fit changes, but these are easy to deal with in the search software. Using this technique results in a smaller number of model fits compared to the cost minimization technique, since a much smaller range of w is searched.

Figures 3 and 7 show analysis of the same data with different values of w. In Fig. 3, $w = 0$ m s^{-1}, while in Fig. 7 $w = 0.130$ m s^{-1} as determined using the $D_m(Z)$ method. Comparison of the goodness-of-fit cost functions between the two retrievals shows both of the resulting models closely fit the data. These two solutions are marked with dashed lines in Figs. 4, 5, and 6. The cost functions shown in Fig. 4 have minima in the 0.0 to 0.5 m s^{-1} region, containing both selected retrievals. We have shown three possible methods to determine $N_{GGD}(D)$ from a power spectra of observed data: 1) assume $w = 0$; 2) assume the observed DSD is described by a generalized gamma distribution, then search different values of w for a minimum in some cost function; and 3) assume D_m and Z are related, then use the $D_m(Z)$ relationship and search for a value of w that matches this value of D_m based on the observed Z. Using the $D_m(Z)$ selection technique connects the solution to an observable quantity, allowing the vertical air velocity to be determined from the data. A fourth method would be to get w from some other source, such as a direct measurement of w. For the rest of this manuscript we use the $D_m(Z)$ method to determine the vertical air velocity, w. Note that the $D_m(Z)$ method was used in the example retrieval shown in Fig. 2.

5. Large population data descriptions

More verification of the assumptions used to obtain these results is required to fully validate this approach. With this caveat, the estimated quantities provide insight into precipitation vertical structure observed by the HPSLR. Figure 8 shows the reflectivity factor in dBZ in the lowest 5 km for the whole

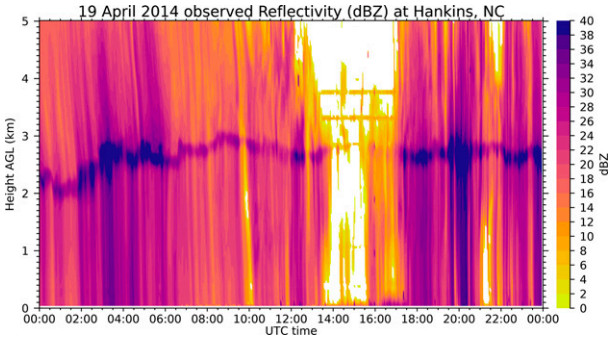

FIG. 8. Reflectivity for the Hankins HPSLR on 19 Apr 2014. This shows the calibrated data used in this analysis.

day of 19 April 2014 (time is UTC). The radar bright band ranges between 2 and 3 km. To avoid brightband contamination, only spectra below 2 km and with reflectivity larger than 0 dBZ are used in the DSD retrievals. There are 574 different dwell periods and 50 heights, providing 28 700 possible members of the population. Of these 1615 did not have adequate reflectivity or number of spectral points to attempt a retrieval, giving a possible population of 27 085 spectra for possible DSD retrievals.

Using the $D_m(Z)$ method, specific fits for each height and dwell can be determined (except where the data do not support a solution). Figure 9 shows histograms of the fit parameters μ, Λ, and c, with minimal quality control of the data. For Figs. 9–14, retrievals that did not converge, or had values $\mu \geq 200$, or $c < 0$, or $N_0 \leq 0$, or $\Lambda \geq 5000$ are excluded from the analysis. Of the possible 27 085 retrievals, 463 (1.7%) are excluded. These generous limits remove very little of the data. In the future the limits of these parameters may be refined but at this point there is no justification to remove more data.

Figure 10 shows a histogram of the χ^2 values. The χ^2 value is a measure of how well the model matches the data. The mean χ^2 is 8.9 and median is 4.7. There 3213 (12%) χ^2 values not shown on the plot, with the largest value of $\chi^2 = 251$.

These results appear to represent realistic geophysical quantities, which is the goal of this study. Figure 11 shows the vertical air velocity w estimated from the observations. The vertical air vertical is predominately upward, as seen in the histogram of the vertical velocities. This is expected at this site, which is located at the bottom of a ridge perpendicular to the prevailing flow advecting the precipitation toward the ridge.

Figure 12 shows the mean-mass drop diameter D_m estimated from the model DSDs. The time–height contour in the top panel shows D_m changes in time but is nearly constant throughout the column. The histogram of D_m shows values of ~1 mm for the mean and median of the population.

Figure 13 shows the minimum drop sizes $D_{\min}$ determined from the radar observations with w chosen so the $N_{GGD}(D)$ model has a D_m value equal to that obtained using (19). The top panel shows the minimum drop size $D_{\min}$ observed as contours in time height. The bottom panel shows the histogram

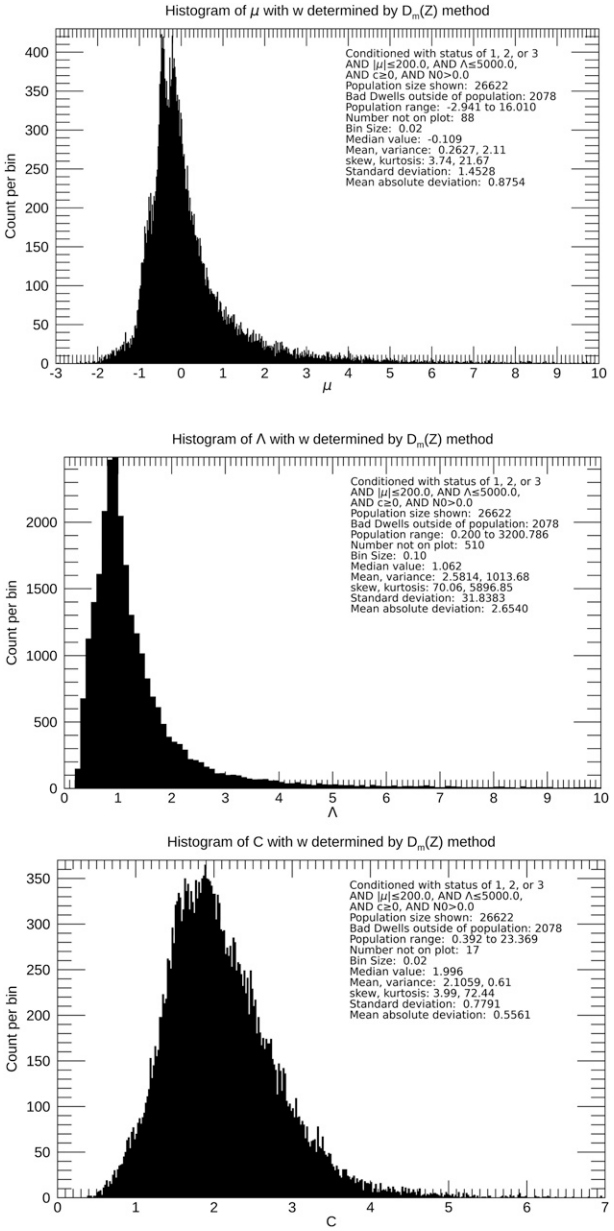

FIG. 9. Histograms of the GGD parameters estimated using data from the Hankins HPSLR on 19 Apr 2014.

of $D_{\min}$. The median observed $D_{\min}$ is 0.17 mm, much smaller than the 0.312 mm minimum drop size observed by the Parsivel[2] disdrometer (Table C1, OTT Hydromet 2016); 95% of the $D_{\min}$ values are 0.3 mm or smaller. The peak at 0.04 mm shows that the radar observes very small drops in many observations of the DSD.

Figure 14 shows the same type of plots as Fig. 13, only for the maximum observed drop size $D_{\max}$. The median $D_{\max}$ is 4.47 mm and there are many solutions with 5.35-mm values. This is the maximum allowed drop size using the fall velocity assumptions of section 2 and shown in Fig. 1. Using 9637 h of 1-min 2DVD disdrometer observations Gatlin et al. (2015)

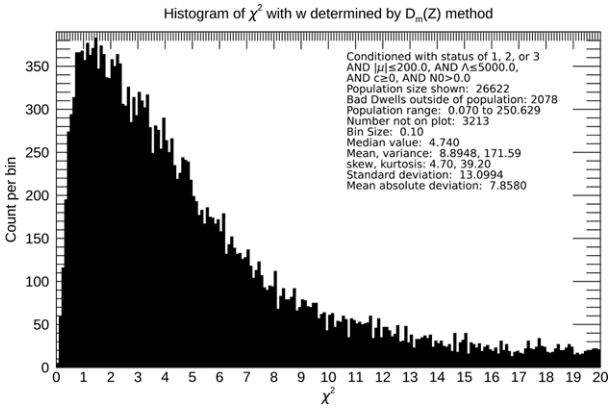

FIG. 10. Histogram of the χ^2goodness-of-fit values for the $D_m(Z)$ method determined GGD models.

found 0.4% of the observations contained drops larger than 5 mm. Looking at the lowest volume observed by the HPSLR (centered 40 m above the surface) 459 DSDs were retrieved. Of these 28, or 6.1%, showed drops larger than 5 mm. Figure 7 shows that the density of 5 mm drops is about 1 drop in 100 m^3. A generous assumption would be that $N(D) = 0.01\ m^{-3}\ mm^{-1}$ over the range of 5 to 8 mm. This would indicate that there should be 1 drop in this size range in a volume of 33 m^3. The 2DVD disdrometers have a collection area of 0.01 m^2. Assuming 9 m s^{-1} fall speed, and 120-s observation period, these disdrometers will observe

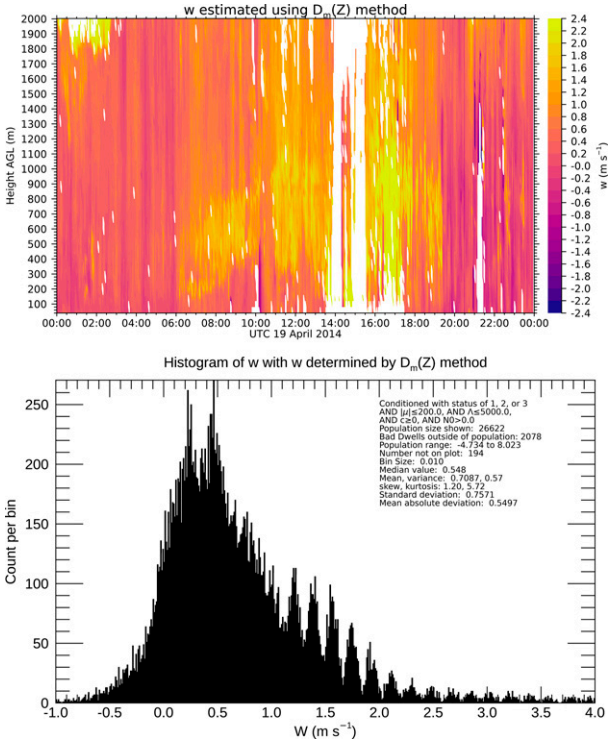

FIG. 11. Vertical clear-air velocity estimated for the observation period.

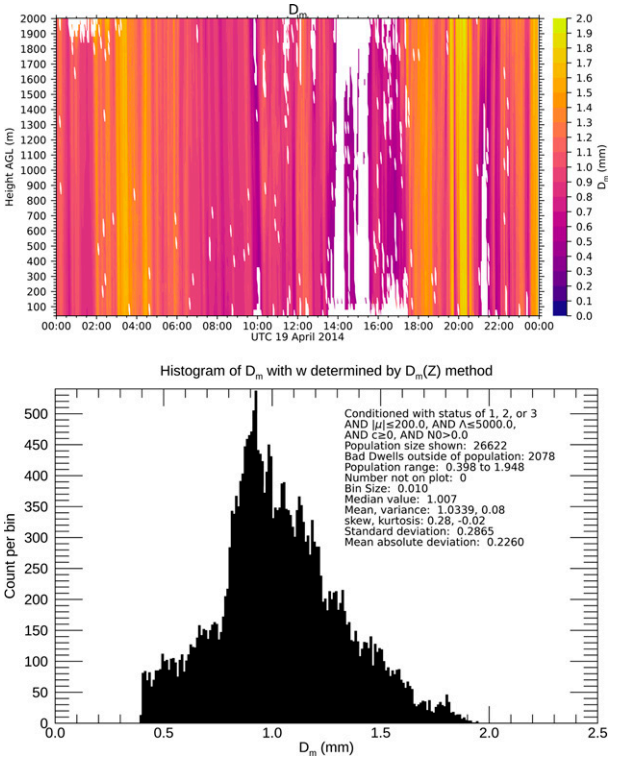

FIG. 12. The mean mass-weighted drop size D_m estimated from GGD fitting of the data from the Hankins HPSLR on 19 Apr 2014. The $D_m(Z)$ method was used to estimate w.

drops from ~10.8-m^3 volume. The first range volume of the HPSLR is ~500 m^3. This large difference in volumes explains most of the reason the disdrometers report few large drops.

6. Discussion

This approach relies on the validity of the $D_m(Z)$ relationship shown in (19). Williams et al. (2014) used ~25 000 2DVD disdrometer observations to determine the relationship in (19). Raupach et al. (2019) show that since D_m and Z are determined by higher-order moments that favor large drop sizes, they are well measured by the 2DVD and OTT Parsivel^2 disdrometers. Further verification of the $D_m(Z)$ relationship needs to be accomplished for full validation of this technique, but for now it provides a way to select a solution for the DSD without knowing the vertical air velocity. Using this relationship allows determination of the DSD and the model $N_{GGD}(D)$ based on a measured value of Z. The cost functions then provide a indication of how well the data are described by the GGD.

Thurai et al. (2019) and Raupach et al. (2019) argue that 2DVDs miss a significant number of small drops, known as the drizzle mode (diameter range from 0.001 to 0.5 mm). Figure 13 shows the smallest drops retrieved from the HPSLR data range from 0.021 to 1.127 mm. More than 96% of the smallest drop sizes retrieved are less than 0.312 mm, the smallest drop observed with the Parsivel disdrometer.

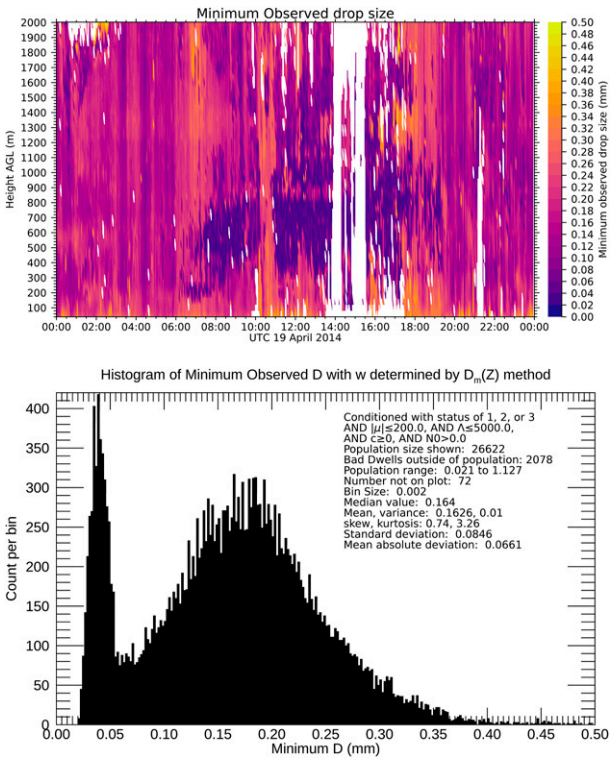

FIG. 13. Minimum observed drop size $D_{\min}$.

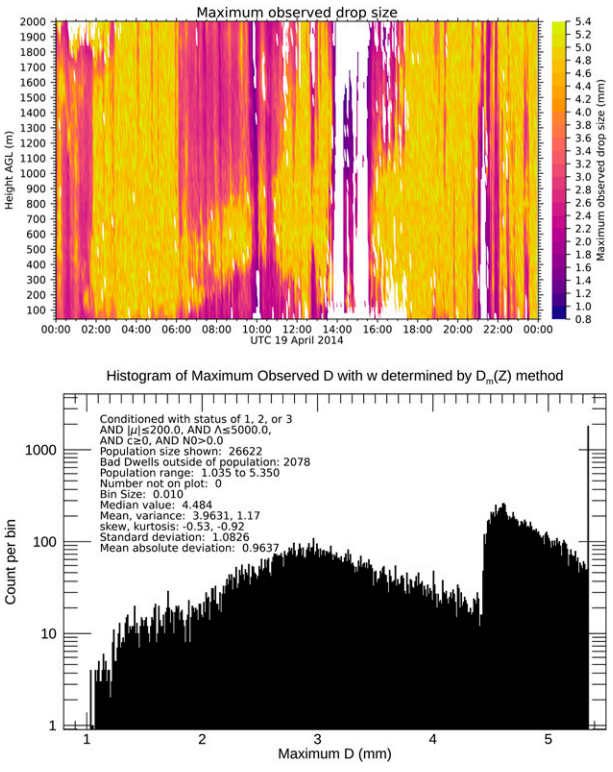

FIG. 14. Maximum observed drop size $D_{\max}$.

Figures 2, 3, and 7 show retrievals with an increasing number of drops as the drop size decreases; consistent with the Raupach et al. (2019) description of the drizzle mode.

In this analysis, the spectral width or turbulence was not utilized. Many investigators use some turbulence characterization to modify the input spectra, to compensate for turbulent and finite beam effects on the fall velocity. This has a second-order effect on DSD estimation (Rajopadhyaya et al. 1998) and is not utilized in this analysis. In the mean, the turbulence averages to zero, so that the observations reflect the mean fall speed. The turbulence measured by the radar in clear air is one component of the turbulent spectrum, where the radar wavelength meets the Bragg-scatter condition. This may not represent the full turbulence affecting the falling drops. The momentum of large drops is quite different than that of small drops, so could be affected differently. Nijhuis et al. (2016) discuss this issue and show that turbulence inertia is important for impacting different drop sizes differently. Peters et al. (2005) present a technique to separate out the turbulence contribution to the spectra by utilizing geometric averaging of the power spectra and comparing the results with the standard incoherent averaging of power spectra.

The GGD appears to be a good descriptor of the DSDs observed using a vertically pointing S-band radar. The HPSLR has enough sensitivity to observe small drops. Our analysis shows the existence of the drizzle mode ($D \leq 0.5$ mm) that is not observed with most other in situ instruments, such as impact or video disdrometers. Our measurements are consistent with the measurements of Thurai et al. (2019) obtained using a Meteorological Particle Spectrometer to observe drops as small as 50 μm diameter. Observations of the drizzle mode have also been reported using K-band MRRs by Adirosi et al. (2016) and Jash et al. (2019).

The works by Thurai and Bringi (2018) and Raupach et al. (2019) suggest that DSDs can be described using universal values of the parameters μ and c. Do our results support these assertions? The histograms of μ, Λ, and c show narrow distributions suggesting that, indeed, there may be "universal" parameters that can be used to accurately describe DSDs. Our results are from one day at one site, not enough to establish a universal distribution. This is certainly an area for further research.

The retrievals presented here have undergone minimal quality controls. There are 28 700 possible values in our data (574 time periods, 50 heights). Of these, 2078 values have been excluded for some reason, leaving 26 622 retrievals. These are probably not all good retrievals. For example, Fig. 10 shows that 3213 large values of χ^2 are not shown on the plot. Large χ^2 values indicate the data are not well represented by the GGD model. This can be caused by poor data or a poor model. Examination of the data yielding the retrievals with the largest χ^2 values show many cases of a large, narrow peak on top of a broad signal. Many of these cases come from heights above 1800 m during the first 3 h of the day. Figure 8 shows these data are near the bright band and probably represent large drops with mixed-phase particles, a case of good data and poor model. Another possible data

quality issue are the large values of w in the 300–600-m region between 0600 and 1200 UTC visible in the top panel of Fig. 11. Both $D_{\min}$ and $D_{\max}$ also show this layer (Figs. 13 and 14), while Z and D_m do not (Figs. 8 and 12). Do these retrievals show physical values, or is the data quality poor? Along with validation of the $D_m(Z)$ relationship establishment of the data quality is necessary to make this technique viable.

Limiting the maximum drop size by using the monotonic part of the Brandes et al. (2002) $v_{\text{fall}}(D)$ relationship does not affect the results in a substantive way. The works by Gatlin et al. (2015) and Raupach et al. (2019) using disdrometers show that while large drops do exist, when using the D^6 moment, the missing drops do not affect the measurements of reflectivity or the DSD significantly.

7. Conclusions

Deriving microphysical properties of precipitation using ground-based remote sensing poses many challenges. Falling raindrops are a collection of random positions and sizes. It is very difficult, if not impossible, to have multiple measurements of the same collection of drops. This means that the comparisons required to verify measurements must be made with statistical means and not by multiple measurements of the same set of drops. Differences in sampling volume, spatial and temporal resolution, and the low probability of precipitation occurring in the field of view of multiple instruments pose additional difficulties to making high-quality precipitation measurement comparisons.

In this paper, velocity spectra of precipitating particles are measured by S-band vertically pointing radars. By assuming a relationship between reflectivity Z and the mean drop size D_m, we present a technique to convert these spectra to drop size distributions (DSDs) without the measurement of the vertical air velocity. Additional evaluation of this $D_m(Z)$ relationship is critical to verify this technique further. If the $D_m(Z)$ relationship can be further verified, then it will be possible to use well-calibrated vertical profilers to estimate DSDs.

Verification of the $D_m(Z)$ relationship can be accomplished by direct comparison of the DSDs from radars with collocated disdrometers. Disdrometer data can also be utilized to directly verify $D_m(Z)$. Operation of a HPSLR near a wind-profiling radar capable of measuring the vertical air velocity could help verify the vertical air motions obtained by this technique. The data presented are predominately stratiform in nature, where $w \approx 0$. Examination of convective data where $w \neq 0$ will also help to fully evaluate this technique. More radar and disdrometer data are available and will be used in future research to provide estimates of the accuracy and precision of these measurements.

Operation at nonattenuating frequencies eliminates the requirement of measuring or estimating the attenuation of the signal through the medium. This technique should work with UHF (915 and 449 MHz) wind profilers, where direct measurement of the vertical air motion is a possibility. In reality, the drizzle mode can overlap the vertical air motion signal making this a difficult measurement. Additionally, Fig. 6 shows that D_m changes approximately 3 mm over the 6 m s^{-1} range of vertical air velocity, giving a slope ~0.5 mm (m s^{-1})$^{-1}$. To measure D_m to 0.05 mm (~5%) levels will require vertical velocity accuracies of ~0.1 m s^{-1}, which are difficult measurements to achieve.

Radar backscatter cross section is proportional to D^6. Many small drops are required to have the same backscatter cross section as a few large drops. Large sample volumes provide enough small drops to achieve detectable signal levels. Large drops are easily observed but have very low concentrations. Large sample volumes increase to likelihood of the existence of large drops in the observation. The HPSLR has large sample volumes with enough sensitivity to observe both smaller and larger drops that typically are not measured with most disdrometers.

The HPSLR is not a perfect instrument; improvements can be made that would improve DSD retrievals. As seen in Fig. 8, there are instrument artifacts in the upper gates that appear as lines that are constant in height and reflectivity. Improvements are needed to be made in ground clutter reduction, so the small drops can be better observed at low velocities. An increased number of spectral points may help this problem and will also improve the resolution of the large drops. The histogram of vertical air velocity, Fig. 11, shows peaks occurring with the velocity point spacing, suggesting that increased spectral resolution could be useful. Using shorter dwell periods is another improvement we are considering, since we have observed that 2 min is a long time in some precipitation environments. Increasing the range resolution can be easily done. For example, recent observations with this instrument have been taken using 30-m vertical resolution.

One area omitted in this manuscript is a discussion about the uncertainties in the measurements. The use of the $D_m(Z)$ relationship requires an accurate calibration of the radar. A calibration error in the radar reflectivity factor will give an error in the D_m value. These errors can be estimated, with a 1-dB reflectivity error giving less than 4.2% error in D_m. A 3-dB reflectivity error will give less than a 13% error in D_m. It is not unreasonable to $D_m(Z)$ to have some spread about the function we utilize, which will also increase the uncertainties in the measurements. Evaluation and estimation of the uncertainties associated with this technique for estimating the DSD requires more observations, analysis, and comparison with collocated observations from other instruments. We recognize that uncertainties in measurements are important and hope to address this topic in future works.

The results we present are preliminary, subject the validation of our assumptions. One important result from this work is more evidence that there are small drops observed that constitute the "drizzle" mode part of the drop-size spectrum. Our work supports the idea that the generalized gamma distribution (GGD) can be used to describe the DSD.

Acknowledgments. We are grateful for the work of Tom Ayers, Clark King, and Jesse Leach for deploying, operating, and maintaining the HPSLR installation at Hankins,

North Carolina, as part of the HMT-SE experiment. We thank Elizabeth Thompson and Alexander Voronovich of NOAA Physical Sciences Laboratory for reading this manuscript and providing thoughtful comments that greatly improved this work. We also thank the anonymous reviewers for their efforts. Their thoughtful reviews have enhanced this manuscript. This work was supported in part by the NOAA Cooperative Agreement with CIRES, NA17OAR4320101, and by the NOAA Physical Sciences Laboratory.

Data availability statement. The primary dataset used in this paper is too large to make publicly available with available resources. Radar Doppler spectral data are collected and archived in a binary format and are not readily accessible without a binary unpacking routine available from NOAA/PSL. For more information, contact webmaster.psl@noaa.gov or psl.data@noaa.gov.

REFERENCES

Adirosi, E., L. Baldini, N. Roberto, P. Gatlin, and A. Tokay, 2016: Improvement of vertical profiles of raindrop size distribution from Micro Rain Radar using 2D video disdrometer measurements. *Atmos. Res.*, **169**, 404–415, https://doi.org/10.1016/j.atmosres.2015.07.002.

Atlas, E., R. C. Srivastata, and R. S. Sekhon, 1973: Doppler radar characteristics of precipitation at vertical incidence. *Rev. Geophys.*, **11**, 1–35, https://doi.org/10.1029/RG011i001p00001.

Beard, K. V., 1985: Simple altitude adjustments to raindrop velocities for Doppler radar analysis. *J. Atmos. Oceanic Technol.*, **2**, 468–471, https://doi.org/10.1175/1520-0426(1985)002<0468:SAATRV>2.0.CO;2.

Bradley, E. F., and C. W. Fairall, 2006: A guide to making climate quality meteorological and flux measurements at sea. NOAA Tech. Memo. OAR PSD-311, 44 pp.

Brandes, E. A., G. Zhang, and J. Vivekanandan, 2002: Experiments in rainfall estimation with a polarimetric radar in a subtropical environment. *J. Appl. Meteor.*, **41**, 674–685, https://doi.org/10.1175/1520-0450(2002)041<0674:EIREWA>2.0.CO;2.

Carter, D. A., K. S. Gage, W. L. Ecklund, W. M. Angevine, P. E. Johnston, A. C. Riddle, J. Wilson, and C. R. Williams, 1995: Developments in UHF lower tropospheric wind profiling at NOAA's Aeronomy Laboratory. *Radio Sci.*, **30**, 977–1001, https://doi.org/10.1029/95RS00649.

COESA, 1976: *U.S. Standard Atmosphere*, 1976. NOAA, 227 pp.

Currier, P. E., S. K. Avery, B. B. Balsley, K. S. Gage, and W. L. Ecklund, 1992: Combined use of 50 MHz and 915 MHz wind profilers in the estimation of raindrop size distributions. *Geophys. Res. Lett.*, **19**, 1017–1020, https://doi.org/10.1029/92GL00191.

Foote, G. B., and P. S. Du Toit, 1969: Terminal velocity of raindrops aloft. *J. Appl. Meteor.*, **8**, 249–253, https://doi.org/10.1175/1520-0450(1969)008<0249:TVORA>2.0.CO;2.

Gatlin, P. N., M. Thurai, V. N. Bringi, W. Petersen, D. Wolff, A. Tokay, L. Carey, and M. Wingo, 2015: Searching for large raindrops: A global summary of two-dimensional video disdrometer observations. *J. Appl. Meteor. Climatol.*, **54**, 1069–1089, https://doi.org/10.1175/JAMC-D-14-0089.1.

Gunn, R., and G. D. Kinzer, 1949: The terminal velocity of fall for water droplets in stagnant air. *J. Meteor.*, **6**, 243–248, https://doi.org/10.1175/1520-0469(1949)006<0243:TTVOFF>2.0.CO;2.

Hartten, L. M., P. E. Johnston, V. M. Rodríguez Castro, and P. S. Esteban Pérez, 2019: Postdeployment calibration of a tropical UHF profiling radar via surface- and satellite-based methods. *J. Atmos. Oceanic Technol.*, **36**, 1729–1751, https://doi.org/10.1175/JTECH-D-18-0020.1.

Jash, D., E. A. Resmi, C. K. Unnikrishnan, R. K. Sumesh, T. S. Sreekanth, N. Sukumar, and K. K. Ramachandran, 2019: Variation in rain drop size distribution and rain integral parameters during southwest monsoon over a tropical station: An inter-comparison of disdrometer and Micro Rain Radar. *Atmos. Res.*, **217**, 24–36, https://doi.org/10.1016/j.atmosres.2018.10.014.

Johnston, P. E., J. R. Jordan, A. B. White, D. A. Carter, D. M. Costa, and T. E. Ayers, 2017: The NOAA FM-CW snow-level radar. *J. Atmos. Oceanic Technol.*, **34**, 249–267, https://doi.org/10.1175/JTECH-D-16-0063.1.

Markwardt, C. B., 2009: Non-linear least squares fitting in IDL with MPFIT. *18th Annual Conf. on Astronomical Data Analysis Software and Systems*, Quebec City, QC, Canada, Astronomical Society of the Pacific, 251–254.

Marshall, J. S., and W. M. K. Palmer, 1948: The distribution of raindrops with size. *J. Meteor.*, **5**, 165–166, https://doi.org/10.1175/1520-0469(1948)005<0165:TDORWS>2.0.CO;2.

——, R. C. Langille, and W. M. K. Palmer, 1947: Measurement of rainfall by radar. *J. Meteor.*, **4**, 186–192, https://doi.org/10.1175/1520-0469(1947)004<0186:MORBR>2.0.CO;2.

——, W. Hitschfeld, and K. L. S. Gunn, 1955: Advances in radar weather. *Adv. Geophys.*, **2**, 1–56, https://doi.org/10.1016/S0065-2687(08)60310-6.

Nijhuis, A. C. P. O., F. J. Yanovsky, O. Krasnov, C. M. H. Unal, H. W. J. Russchenberg, and A. Yarovoy, 2016: Assessment of the rain drop inertia effect for radar-based turbulence intensity retrievals. *Int. J. Microwave Wireless Technol.*, **8**, 835–844, https://doi.org/10.1017/S1759078716000660.

OTT Hydromet, 2016: Operating instructions present weather sensor OTT Parsivel2. OTT Hydromet Doc. 12-1016, 52 pp., https://www.psl.noaa.gov/data/obs/instruments/OpticalDisdrometerV2.pdf.

Peters, G., B. Fischer, H. Münster, M. Clemens, and A. Wagner, 2005: Profiles of raindrop size distributions as retrieved by Microrain Radars. *J. Appl. Meteor.*, **44**, 1930–1949, https://doi.org/10.1175/JAM2316.1.

Press, W. H., S. A. Teukolsky, W. T. Vetterling, and B. P. Flannery, 1992: *Numerical Recipes in C: The Art of Scientific Computing.* 2nd ed. Cambridge University Press, 994 pp.

Rajopadhyaya, D. K., P. T. May, R. C. Cifelli, S. K. Avery, C. R. Willams, W. L. Ecklund, and K. S. Gage, 1998: The effect of vertical air motions on rain rates and median volume diameter determined from combined UHF and VHF wind profiler measurements and comparisons with rain gauge measurements. *J. Atmos. Oceanic Technol.*, **15**, 1306–1319, https://doi.org/10.1175/1520-0426(1998)015<1306:TEOVAM>2.0.CO;2.

Raupach, T. H., M. Thurai, V. N. Bringi, and A. Berne, 2019: Reconstructing the drizzle mode of the raindrop size distribution using double-moment normalization. *J. Appl. Meteor. Climatol.*, **58**, 145–164, https://doi.org/10.1175/JAMC-D-18-0156.1.

Stacy, E. W., 1962: A generalization of the gamma distribution. *Ann. Math. Stat.*, **33**, 1187–1192, https://doi.org/10.1214/aoms/1177704481.

Tapiador, F. J., Z. S. Haddad, and J. Turk, 2014: A probabilistic view on raindrop size distribution modeling: A physical interpretation of rain microphysics. *J. Hydrometeor.*, **15**, 427–443, https://doi.org/10.1175/JHM-D-13-033.1.

Thurai, M., and V. N. Bringi, 2005: Drop axis ratios from a 2D video disdrometer. *J. Atmos. Oceanic Technol.*, **22**, 966–978, https://doi.org/10.1175/JTECH1767.1.

——, and ——, 2018: Application of the generalized gamma model to represent the full rain drop size distribution spectra. *J. Appl. Meteor. Climatol.*, **57**, 1197–1210, https://doi.org/10.1175/jamc-d-17-0235.1.

——, P. Gatlin, V. N. Bringi, W. Petersen, P. Kennedy, B. Notaroš, and L. Carey, 2017: Toward completing the raindrop size spectrum: Case studies involving 2D-video disdrometer, droplet spectrometer, and polarimetric radar measurements. *J. Appl. Meteor. Climatol.*, **56**, 877–896, https://doi.org/10.1175/JAMC-D-16-0304.1.

——, V. Bringi, P. N. Gatlin, W. A. Petersen, and M. T. Wingo, 2019: Measurements and modeling of the full rain drop size distribution. *Atmosphere*, **10**, 39, https://doi.org/10.3390/atmos10010039.

Ulbrich, C. W., 1983: Natural variations in the analytical form of the raindrop size distribution. *J. Climate Appl. Meteor.*, **22**, 1764–1775, https://doi.org/10.1175/1520-0450(1983)022<1764:NVITAF>2.0.CO;2.

Williams, C. R., 2002: Simultaneous ambient air motion and raindrop size distributions retrieved from UHF vertical incident profiler observations. *Radio Sci.*, **37**, 1024, https://doi.org/10.1029/2000RS002603.

——, and K. S. Gage, 2009: Raindrop size distribution variability estimated using ensemble statistics. *Ann. Geophys.*, **27**, 555–567, https://doi.org/10.5194/angeo-27-555-2009.

——, and Coauthors, 2014: Describing the shape of raindrop size distributions using uncorrelated raindrop mass spectrum parameters. *J. Appl. Meteor. Climatol.*, **53**, 1282–1296, https://doi.org/10.1175/JAMC-D-13-076.1.